

Approximate Quadraticization of High-Order Hamiltonians for Combinatorial Quantum Optimization

Sabina Drăgoi,^{1,2} Alberto Baiardi,² and Daniel J. Egger²

¹*Institute for Theoretical Physics, ETH Zürich, Wolfgang-Pauli-Str. 27, 8093 Zürich, Switzerland*

²*IBM Quantum, IBM Research - Zurich, Säumerstrasse 4, 8803 Rüschlikon, Switzerland*

Combinatorial optimization problems have wide-ranging applications in industry and academia. Quantum computers may help solve them by sampling from carefully prepared Ansatz quantum circuits. However, current quantum computers are limited by their qubit count, connectivity, and noise. This is particularly restrictive when considering optimization problems beyond the quadratic order. Here, we introduce Ansätze based on an approximate quadraticization of high-order Hamiltonians which do not incur a qubit overhead. The price paid is a loss in the quality of the noiseless solution. Crucially, this approximation yields shallower Ansätze which are more robust to noise than the standard QAOA one. We show this through simulations of systems of 8 to 16 qubits with variable noise strengths. Furthermore, we also propose a noise-aware Ansatz design method for quadratic optimization problems. This method implements only part of the corresponding Hamiltonian by limiting the number of layers of SWAP gates in the Ansatz. We find that for both problem types, under noise, our approximate implementation of the full problem structure can significantly enhance the solution quality. Our work opens a path to enhance the solution quality that approximate quantum optimization achieves on noisy hardware.

I. INTRODUCTION

Quantum computing offers a new information-processing framework based on the laws of quantum physics. For certain tasks, quantum computing achieves better performance than the best known classical methods. Famously, Shor’s algorithm delivers an exponential speed-up in factoring over the best known classical algorithms [1]. However, this remains a theoretical feat since Shor’s algorithm requires deep circuits which cannot be faithfully implemented at practically relevant scales on current hardware due to noise. This has motivated the development of algorithms requiring shallow circuits such as Variational Quantum Algorithms (VQAs) [2]. VQAs are heuristic in nature and are often designed to find the ground state of a Hamiltonian [3–5]. VQAs optimize a parametrized quantum circuit called the Ansatz using a classical optimization procedure to update the parameters.

The Ansatz in a VQA can be either problem-agnostic [6] or retain the structure of the problem to solve [7]. Problem-agnostic Ansätze are typically designed to minimize the effect of noise by accounting for hardware constraints. However, they come at the cost of limited expressivity compared to Ansätze that fully encode the problem structure. Designing expressive and shallow Ansätze remains an open question [8].

Here, we focus on VQAs to solve combinatorial optimization problems, which are prevalent across industry applications such as communication [9], finance [10, 11], and vehicle routing [12–14]. Many relevant combinatorial optimization problems are hard to solve exactly [15]. In addition, some of them also do not have polynomial-time approximate algorithms that reach an arbitrarily accurate approximation of the optimal solution [16]. Therefore, many classical algorithms designed to solve such

problems are heuristic in nature. Crucially, they work well in practice, thus motivating a similar heuristic approach for quantum computing [17].

A foundational VQA for combinatorial optimization problems is the Quantum Approximate Optimization Algorithm (QAOA) [18, 19]. Its trotterized Ansatz structure alternates p time evolutions of the target problem and of a problem-independent Hamiltonian. The structure is inspired from the adiabatic theorem in physics, and thus inherits its convergence guarantee in the limit $p \rightarrow \infty$ [18, 20, 21].

Finite-depth QAOA is a heuristic algorithm, which implies that its performance must be thoroughly investigated and benchmarked on a case-by-case basis [17, 22]. In particular, research often investigates QAOA for quadratic unconstrained binary optimization problems (QUBOs), such as Max-Cut, to benchmark hardware performance [23–26] and validate new algorithms [27, 28]. However, Max-Cut can often easily be exactly solved classically at low graph densities and up to 10 000 nodes [29]. Solving it using QAOA would only yield approximate solutions even in an ideal case [30–33], thus making it a poor candidate to deliver a quantum advantage. Hence, recent studies investigated high-order unconstrained binary optimization problems (HUBOs) with cubic and quartic terms. Certain HUBOs can be very hard to solve, even at a low number of decision variables [34]. For instance, the largest exactly solved instance of the Low Autocorrelation Binary Sequence (LABS) problem has only 66 decision variables [35, 36]. Importantly, Ref. [37] suggests a scaling advantage for QAOA over Gurobi [38] or CPLEX [39] in solving LABS.

In this work, we first show in Section II how the quantum resources requirements of QAOA scale unfavorably for HUBOs by considering two test cases: a fully-connected four-local Hamiltonian, and the LABS problem. Next, we introduce in Section III an approximate

quadratzation procedure to reduce the QAOA circuit depth without additional qubits. Motivated by the idea of approximating the circuit Ansatz associated with a given problem, we benchmark how simplifications in the QAOA Ansatz improve measured approximation ratios when executing Max-Cut on hardware in Section IV. Finally, in Section V, we argue for the need of a more mathematically motivated quadratzation and suggest some ideas in this direction.

II. EXECUTING QAOA ON DIGITAL QUANTUM COMPUTERS

We consider combinatorial optimization problems defined over n binary variables $x \in \{0, 1\}^n$ which minimize an objective function $f(x)$. Quantum computers can tackle such problems by mapping $f(x)$ to an Ising Hamiltonian H_C whose ground state minimizes $f(x)$. This is done through the change of variables $x_i = \frac{1-z_i}{2}$ and promoting z_i to Pauli Z operators Z_i [40]. Then, we use QAOA to find the ground state of H_C by sampling from an Ansatz

$$|\psi(\beta, \gamma)\rangle = \prod_{q=1}^p e^{-i\beta_q H_M} e^{-i\gamma_q H_C} |+\rangle^{\otimes n} \quad (1)$$

with optimized variational parameters (β, γ) . Here, we consider a problem-independent mixer operator $H_M = -\sum_{i=0}^{n-1} X_i$, although other mixing Hamiltonians have been developed to enforce constraints or leverage warm-starts [28, 41–45].

QUBOs are unconstrained combinatorial optimization problems with a polynomial $f(x)$ of degree at most two. As such, their cost Hamiltonian is expressible as

$$H_{\text{QUBO}} = \sum_{j < k} w_{jk} Z_j Z_k + \sum_j w_j Z_j. \quad (2)$$

The main challenge associated with running QAOA on hardware is implementing the time evolution of the cost Hamiltonian. In particular, the more terms H_C contains, the denser and deeper the resulting circuits become, which results in noisier samples. The maximum number of gates in the corresponding circuit of a fully-connected QUBO H_2^{full} scales as $O(n^2)$, with a $O(n)$ two-qubit gate depth¹, see the purple lines in Fig. 1. When transpiled to a line of qubits the complexity exponent stays the same, but the constant factor increases by 1.45 due to the additional SWAP gates required to reach all-to-all connectivity, see details in App. A and B 1.

¹ We only consider two-qubit gates in gate counts as these are the main source of errors. For instance, the median error rates of the CZ gates is $8.30 \cdot 10^{-3}$, compared to $2.23 \cdot 10^{-4}$ for single-qubit gates on *ibm_fez*. Similarly, when computing circuit depth, we refer only to the depth required to implement two-qubit gates.

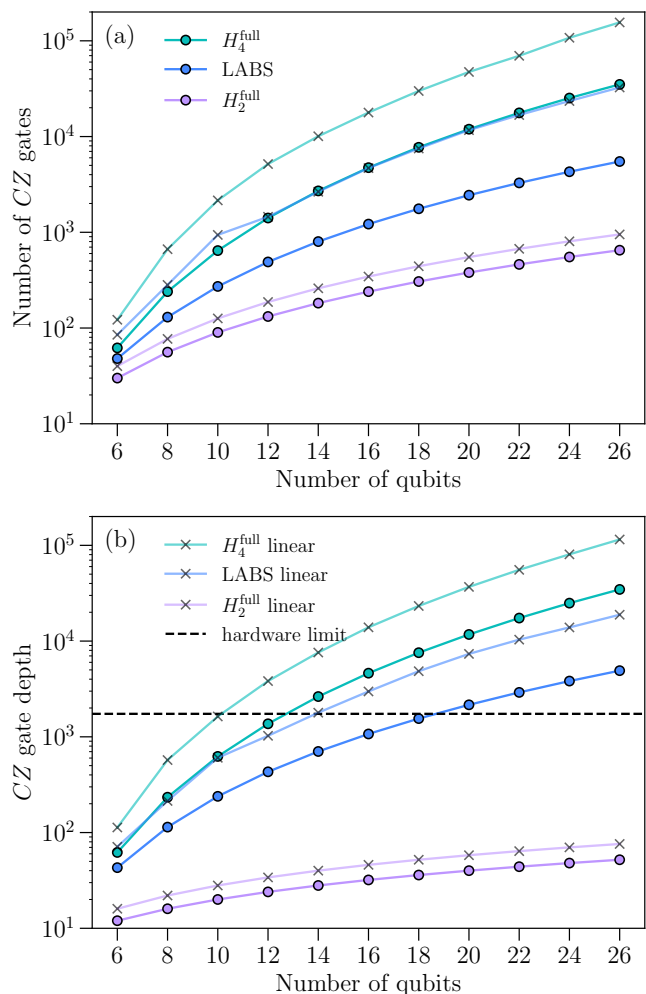


Figure 1. Circuit complexity of $e^{-i\gamma H_C}$ for H_4^{full} (teal) and LABS (blue) compared to a fully-connected QUBO (purple). Panel (a) shows the number of CZ gates as a function of problem size. Panel (b) shows the CZ gate depth of the transpiled circuits. The continuous lines connect raw data points. The horizontal dashed line corresponds to the number of CZ gates that fit within the median qubit T_1 time on *ibm_fez*.

Furthermore, the locality of the gates in $\exp(-i\gamma H_C)$ significantly impacts the circuit depth. A gate $\exp(-i\gamma Z_j Z_k)$ is implemented by a single R_{ZZ} rotation if the qubits j and k are connected on the hardware. Otherwise, additional SWAP gates are needed to bring qubits j and k in contact. Minimizing the SWAP overhead is desirable since each SWAP gate is built from three noisy entangling gates. Implementing $\exp(-i\gamma H_C)$ is even more challenging for HUBOs, whose terms require more stringent connectivity constraints, i.e. implementing $\exp(-i\gamma Z_j Z_k Z_l Z_h)$ requires connecting qubits (j, k, l, h) . Therefore, HUBOs are more complicated to implement than QUBOs as they require implementing possibly many non-local gates. We now investigate the gate count and depth for the LABS problem and a fully-connected fourth-order Hamiltonian H_4^{full} .

Problem	4 th order terms		2 nd order terms		All-to-all connectivity		Linear connectivity	
	scaling	$n = 16$	scaling	$n = 16$	# CZ gates	CZ gate depth	# CZ gates	CZ gate depth
H_2^{full}	-	-	$O(n^2)$	120	240	32	507	103
LABS	$O(n^3)$	252	$O(n^2)$	56	1218	1071	4685	2978
H_4^{full}	$O(n^4)$	1820	-	-	4732	4622	17813	13920

Table I. Complexity scaling of selected problems. The trends in the first and third columns are shown in Fig. 1. The numerical values in the remaining columns correspond to problem instances with 16 variables.

The LABS problem has applications in signal-processing [46] and statistical physics [47]. It aims to minimize the sidelobe energy

$$\mathcal{E}_{\text{sidelobe}} = \sum_{k=1}^{n-1} C_k(z)^2 \quad (3)$$

of a length n spin sequence $z \in \{-1, 1\}^n$. Here, the autocorrelation functions are

$$C_k(z) = \sum_{i=1}^{n-k} z_i z_{i+k}. \quad (4)$$

Expanding the sums in the expression of the sidelobe energy yields the Hamiltonian [37]

$$\begin{aligned} H_{\text{LABS}} = & 2 \sum_{i=1}^{n-3} Z_i \sum_{t=1}^{\lfloor \frac{n-i-1}{2} \rfloor} \sum_{k=t+1}^{n-i-t} Z_{i+t} Z_{i+k} Z_{i+k+t} \\ & + \sum_{i=1}^{n-2} Z_i \sum_{k=1}^{\lfloor \frac{n-i}{2} \rfloor} Z_{i+2k}. \end{aligned} \quad (5)$$

Solving LABS with QAOA thus requires $O(n^3)$ four-local terms and $O(n^2)$ two-local terms. The dominant $O(n^3)$ scaling is shown by the thicker blue lines in Fig. 1. For example, the largest LABS instance we solve has 16 decision variables, leading to 252 fourth-order terms and 56 second-order terms. This requires $252 \times 6 + 56 \times 2 = 1624$ two-qubit gates assuming an all-to-all connectivity, where the constant factors 6 and 2 are due to the two-qubit gate decomposition, see Figs. 2(a,b). By using the highest optimization level 3 when transpiling with Qiskit, this number reduces to 1218 through cancellation of neighboring two-qubit gates [48]. However, when compiled to linearly connected qubits, the two-qubit gate count increases to 4685 with a two-qubit gate depth of 2978, see the thin blue line in Fig. 1. Implementing such deep circuits on current noisy hardware is a formidable challenge. For instance, on *ibm_fez*, the median T_1 time of 146 μs fits approximately only 1738 layers of two-qubit gates with a median gate time of 84 ns.

The hardest fourth order problem to implement is a fully-connected four-local Hamiltonian H_4^{full} , which has a similar structure as the Sachdev-Kitaev-Ye model of Majorana fermions [49–51], but which is expressed in terms of Pauli operators instead of fermionic ones. Concretely, we define

$$H_4^{\text{full}} = \sum_{j < k < h < l}^{\binom{n}{4}} J_{jklh} Z_j Z_k Z_h Z_l. \quad (6)$$

The weights J_{jklh} are sampled from the standard normal distribution. The resulting circuits have $O(n^4)$ two-qubit gates, and $O(n^3)$ two-qubit gate depth, see teal line in Fig. 1. Implementing QAOA for H_4^{full} is thus more challenging than for LABS, and considerably more so than for a fully-connected QUBO. This is true not just in the asymptotic limit, but also for instances with as few as 16 variables which require 4732 CZ gates and a depth of 4622 assuming all-to-all connectivity, and more than three times as much for a linear qubit topology, see Tab. I.

Finally, these deep circuits result in low sampling rates on hardware. We estimate the rate at which we generate samples by the inverse of the duration of the quantum circuit. Furthermore, we lower bound the duration of a depth-one QAOA with the duration of running $e^{-i\gamma H_C}$, which is the product of the two-qubit gate duration \bar{T} and the two-qubit gate depth. Extrapolating the data in Fig. 1 to a LABS system with 127 qubits, corresponding to one of the largest lines of superconducting qubits available [48], we conclude that we need a two-qubit gate depth of about $8.82 \cdot 10^6$ to implement it. Taking $\bar{T} = 84$ ns, corresponding to the median CZ gate duration of *ibm_fez*, this results in a runtime of 0.741 s per sample. This means that we can generate samples at a rate of at most 1.35 s^{-1} , which is six orders of magnitude slower than the best-known classical methods for the same problem size [52].

III. APPROXIMATE QUADRATIZATION

Compiling quartic HUBO problems to hardware-native instructions results in very deep circuits, while QUBOs are optimally compiled in linear depth with SWAP networks [41, 53]. This motivates us to design a QUBO based on the target HUBO to generate the Ansatz. For example, an exact quadratization that exactly conserves the full structure of the HUBO replaces each four-local term with one constant, four linear, and six quadratic terms at the expense of adding two ancilla qubits per four-local term [54]. This implies that implementing four-local Hamiltonians with $O(n^3)$ terms, such as LABS, or

$O(n^4)$ terms, such as H_4^{full} , requires circuits with a qubit overhead scaling as $O(n^3)$ or $O(n^4)$, respectively. This is impractical due to the limited qubit count of the current hardware. We therefore introduce an *approximate* quadratization to project a generic HUBO onto a QUBO without adding decision variables.

A. Method

We quadratize HUBOs with a hypergraph clique expansion [55]. The price paid to keep the qubit count constant is an approximation of the original problem. We treat a fourth-order Hamiltonian as a hypergraph $\mathcal{G} = (\mathcal{E}, V)$ by identifying each four-local $Z_j Z_k Z_h Z_l$ term with a hyperedge connecting nodes $e = (j, k, h, l) \in \mathcal{E}$. To quadratize H_4 , we create a weighted graph $G = (E, V)$, resulting in a quadratic Hamiltonian H_2 . We add an edge to E for each pair of nodes (j, k) within a hyperedge e , as shown in Fig. 2(c). Therefore, each hyperedge in \mathcal{E} generates a four-clique in G . Since a given pair of nodes (j, k) might belong to multiple hyperedges of \mathcal{E} , the weight $w_2^{\text{opt}}(j, k)$ we assign to it minimizes the l_2 -norm, i.e. the sum of squared differences, with respect to the weights $w_4(e)$ of all hyperedges e that contain (j, k) . The l_2 -norm is chosen according to the quadratization given in the literature [55]. Concretely, for each resulting edge $(j, k) \in E$, we consider the set of hyperedges $\mathcal{E}_{(j,k)}$ that contain the edge (j, k) and choose

$$w_2^{\text{opt}}(j, k) = \arg \min_{w_2(j,k)} \sum_{e \in \mathcal{E}_{(j,k)}} \left(w_2(j, k) - w_4(e) \right)^2. \quad (7)$$

We use the resulting quadratic Hamiltonian

$$H_2 = \sum_{(j,k) \in E} w_2^{\text{opt}}(j, k) Z_j Z_k \quad (8)$$

to generate the Ansatz circuit of QAOA, while still evaluating the objective function with respect to the original quartic Hamiltonian. Concretely, after the circuit prepares a state

$$|\psi_2(\boldsymbol{\beta}, \boldsymbol{\gamma})\rangle = \prod_{q=1}^p e^{-i\beta_q H_M} e^{-i\gamma_q H_2} |+\rangle^{\otimes n}, \quad (9)$$

we minimize the energy $\langle \psi_2(\boldsymbol{\beta}, \boldsymbol{\gamma}) | H_4 | \psi_2(\boldsymbol{\beta}, \boldsymbol{\gamma}) \rangle$.

Our approach introduces an inconsistency between the cost operator and the operator that creates the Ansatz. Therefore, the convergence guarantee of a typical QAOA in the limit $p \rightarrow \infty$ is lost. Instead, we are left with a heuristic approach based on an Ansatz circuit that retains only some of the structure of H_4 , but which considerably reduces the circuit depth. The exact depth reduction depends on the density of the original problem. The largest reduction occurs for dense Hamiltonians, such as H_4^{full} , for which the reduction scales as $O(n^2)$, see Fig. 1. For LABS, which has $O(n^3)$ terms, the reduction factor is $O(n)$.

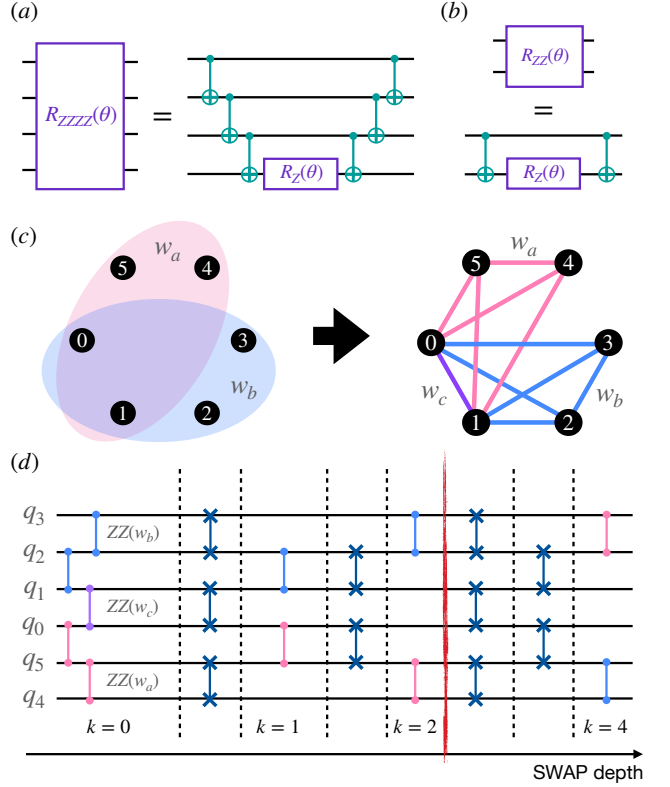


Figure 2. Construction of shallow Ansatz. (a) and (b) show how a four-local gate $\exp(-i\gamma ZZZZ)$ and a two-local gate $\exp(-i\gamma ZZ)$, respectively, decompose into R_Z and CX gates. (c) The hypergraph clique expansion generates a 2D graph that is easier to implement on quantum hardware. The graph is generated such that each pair of nodes in the original hypergraph has a corresponding edge, and the weight of this edge is given by Eq. (7). Here, the edge $(0, 1)$ has weight $w_c = (w_a + w_b)/2$, whereas the other edges preserve the weights of the single hyperedge they correspondingly belong to. (d) Circuit implementation of the resulting graph with layers of SWAP gates. To avoid hardware noise, we skip implementing the last two SWAP layers, at the cost losing some correlation with the original problem.

B. Expected performance of quadratization

We now assess the quadratization by creating a scatter plot of the energies of the quartic Hamiltonian $\langle x | H_4 | x \rangle$ against the energies of the corresponding quadratic Hamiltonian $\langle x | H_2 | x \rangle$, for all basis states x . We perform this assessment on the H_4^{full} and LABS Hamiltonians with 12 decision variables. Based on this analysis, we assess whether it is promising to look at similar problem instances for larger systems, since trends in expected performance change smoothly with system size [56].

We do not observe any correlation between the energy calculated with H_4^{full} and with its quadratized counterpart, see Fig. 3(a). Indeed, both energy distributions are normal and uncorrelated. This implies that all of the problem structure of H_4^{full} is lost in the quadratization.

However, the quadratization of LABS, discussed in App. C, retains some of the problem structure, see Fig. 3(b). This results from a combined effect of the distribution of edge weights and the hyperedge structure of LABS. LABS has all weights equal to either 2 for four-local terms, or 1 for two-local terms. This results in a quadratized QUBO with almost all equal edge weights. As a result, all basis states with Hamming weight $0 \leq h \leq n$ and $n - h$ have almost the same QUBO energy, defining the energies of the vertical clusters in Fig. 3(b). More details on the impact of the problem structure and the edge weight distribution on the scatter plots are given in App. D. There, we also consider Hamiltonians with different structures and hyperedge weight distributions.

Next, we run a depth-one QAOA using both the quartic and quadratic Hamiltonians to generate the Ansatz circuit. To optimize the parameters, we first run an exhaustive search in the space $\beta, \gamma \in [0, \pi/2]$, with a resolution of 60 for both parameters, for a system of 6 qubits. For larger systems, optima are found through successive initialization of the parameters using the optimal values found for a system with one qubit less, see Fig. 4. Details on the parameter optimization procedure are in App. E 1.

In the H_4^{full} case, we find $(\beta, \gamma) = (1.319, 0.046)$ for the standard Ansatz and $(\beta, \gamma) = (1.481, 1.565)$ for the quadratized Ansatz. We confirm through a t-test with 97.7% confidence that the quadratized Ansatz outputs samples that produce the same energy expectation as uniformly sampled solutions, see Fig. 3. In our tests, we ran the circuits 10 times with 10 000 shots each. This confirms that for this Hamiltonian structure and normal hyperedge weight distribution, the QUBO Ansatz does not preserve the structure of the original H_4^{full} problem.

For LABS, the optimized parameters $(\beta, \gamma) = (1.416, 0.028)$ for the standard Ansatz generate better samples than random sampling. The QUBO Ansatz, with optimal parameters $(\beta, \gamma) = (1.480, 0.168)$, yields a worse outcome distribution (mean lowest energy of -3.338) than using the standard Ansatz (mean lowest energy of -9.852), see optimization landscapes in Fig. 4. However, in this case, the QUBO Ansatz performs statistically better than random sampling, indicating that it preserves some of the structure of LABS. Crucially, the quadratic Ansatz has $O(n)$ times less two-qubit gates than the quartic Ansatz. Therefore, the quadratic Ansatz is expected to outperform the standard one under noisy conditions.

C. Noisy simulations

The previous section showed that our proposed clique projection yields, in the noiseless case, an improved energy over random sampling, but not over the original quartic Ansatz. We now study this quadratization for QAOA depths $p = 1$ and 2 for LABS problems with

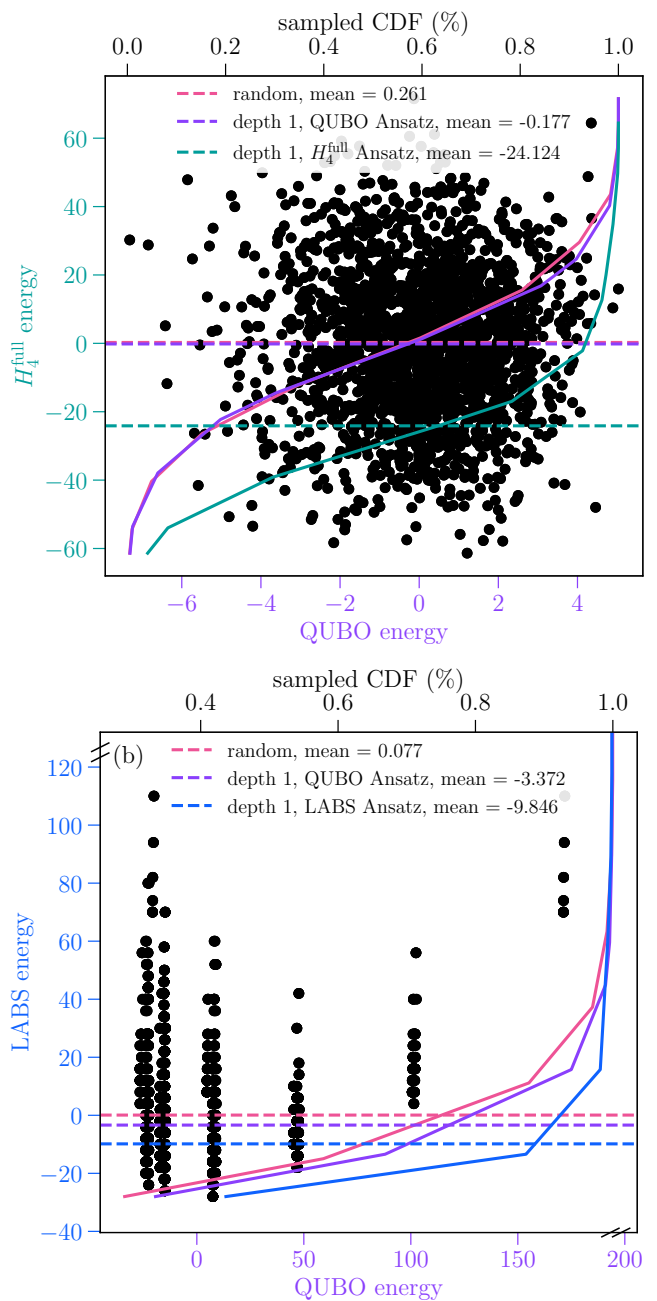


Figure 3. Structure retention in the quadratization. The black dots show the energy of different bitstrings with respect to the quartic Hamiltonian versus the energies with respect to the quadratized Hamiltonian. The curves show the Cumulative Distribution Function (CDF) of the quartic energies of uniform samples (pink), and samples from running QAOA with the quadratized Ansatz (purple), and the standard Ansatz (blue). The horizontal lines show the corresponding mean energies of these distributions. Simulations were done using 10 000 shots resulting in shot noise with a variance of 0.32 for H_4^{full} and 0.18 for LABS.

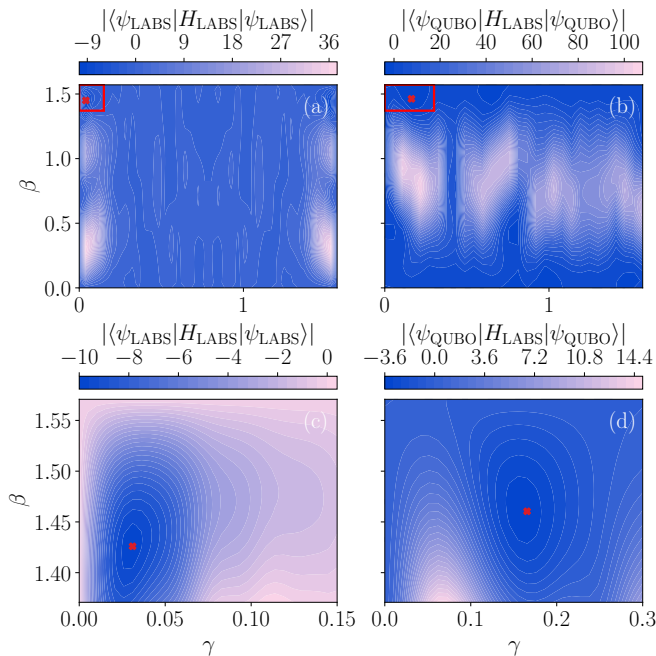


Figure 4. Optimization landscapes of depth-one QAOA for LABS on 12 qubits when using a LABS Ansatz in panels (a) and (c), and using the quadratized Ansatz in panels (b) and (d). Panels (c) and (d) show in more detail the areas in the red squares in panels (a) and (b), respectively. Simulations were done using a statevector simulator and are thus exact.

sizes from $n = 8$ to 16 by simulating the corresponding quantum circuits with and without noise. First, in the absence of noise, as p increases, we observe a decrease in energy for both the quartic and the quadratic Ansatz, see the blue and the purple curves in Figs. 5(a) and (d), respectively. By comparing corresponding pairs of lines from these two subfigures, we see a maximal relative energy improvement brought by adding a QAOA layer of only 13.52% for the LABS Ansatz and 4.78% for the QUBO Ansatz relative to the global minimum value $(-8, -28, -48)$ for 8, 12, and 16 qubits, respectively). This is in part due to the limited performance of a depth-two QAOA, but also due to the more difficult parameter training, which heavily relies on a suitable initialization [57].

We test whether a quadratic Ansatz has a better performance than a quartic one in the presence of noise by setting up a noisy simulation in which we apply a depolarizing channel with strength λ after each hardware-native entangling gate. At $\lambda = 0.001$, depth-one QAOA with a quartic Ansatz outperforms QAOA with a quadratic Ansatz, see Fig. 5(b). However, for problems with more than 13 decision variables, the average energy of the samples drawn from the quartic Ansatz starts increasing. This indicates that the energy gain of a more accurate Hamiltonian is eroded by the noise. This also explains why the depth-two quartic Ansatz, blue line in Fig. 5(e), reverses its downward trend in energy faster than the

depth-one, at $n = 10$ instead of 13. Indeed, depth-two QAOA has twice the gate count of depth-one QAOA. For the 16 qubit systems, depth-two QAOA becomes indistinguishable from random sampling. Extrapolating the trend in Fig. 5(b) we conclude that depth-one QAOA has the same performance as random sampling for problems with more than 30 – 40 decision variables.

The quadratized Ansatz presents more promising scaling prospects, making it a viable option for noisy quantum computers. In contrast to the full LABS Ansatz, the quadratic Ansatz preserves the decreasing energy trend with system size even in the presence of depolarizing noise strength of $\lambda = 0.001$, see purple lines in Figs. 5(b) and (e). Therefore, as the system size increases, the performance gain from the quadratic Ansatz is strong enough to balance the added noise. This feature persists, albeit diminished, even for a stronger noise strength $\lambda = 0.005$, where some signal can still be detected when using the QUBO Ansatz compared to the original Ansatz for $p = 1$, see Figs. 5(c) and (f). However, at $p = 2$, noise completely cancels out the signal for both the full LABS Ansatz and the quadratized Ansatz for all problem sizes tested.

These data show the benefits of quadratizing the Ansatz when working with hardware with small to intermediate noise. In particular, no performance over random sampling is expected from either Ansatz at the current hardware noise levels of $\lambda > 0.01$ [48, 58]. However, our work indicates at which noise level one expects the quadratized Ansatz to outperform its full counterpart.

IV. HARDWARE-NATIVE CIRCUITS FOR QUBOS

We now study an approximate hardware-friendly compilation method of Ansatz circuits for QUBOs. The standard approach to route an arbitrary QAOA circuit utilizes a predetermined network of SWAP gates tailored to the qubit connectivity [41, 53, 60, 61]. We use a line of qubits to benefit from two-qubit gate cancellations, even though the hardware connectivity has a heavy-hex structure [60]. To fully implement $e^{-i\gamma H_C}$, we apply k_{\max} alternating layers of even and odd SWAP layers², see Fig. 2(d). Full connectivity is reached after $n - 2$ SWAP layers. The SWAP network thus allows us to derive an approximate Ansatz by including only $k < k_{\max}$ layers when implementing $e^{-i\gamma H_C}$. Hence, we implement only the time evolution of a subset $H_C(k)$ of the terms in H_C . The truncated $H_C(k)$ is based on the subgraph $G_k = (E_k, V) \subseteq G = (E, V)$. Details on the transpilation are given in App. B2. Importantly, the size $|E_k|$ depends on the initial mapping of the decision variables

² A SWAP layer is a depth-one circuit which applies SWAP gates to pairs of neighboring qubits, and it is called even if the first pair is $(0, 1)$ and odd if it is $(1, 2)$.

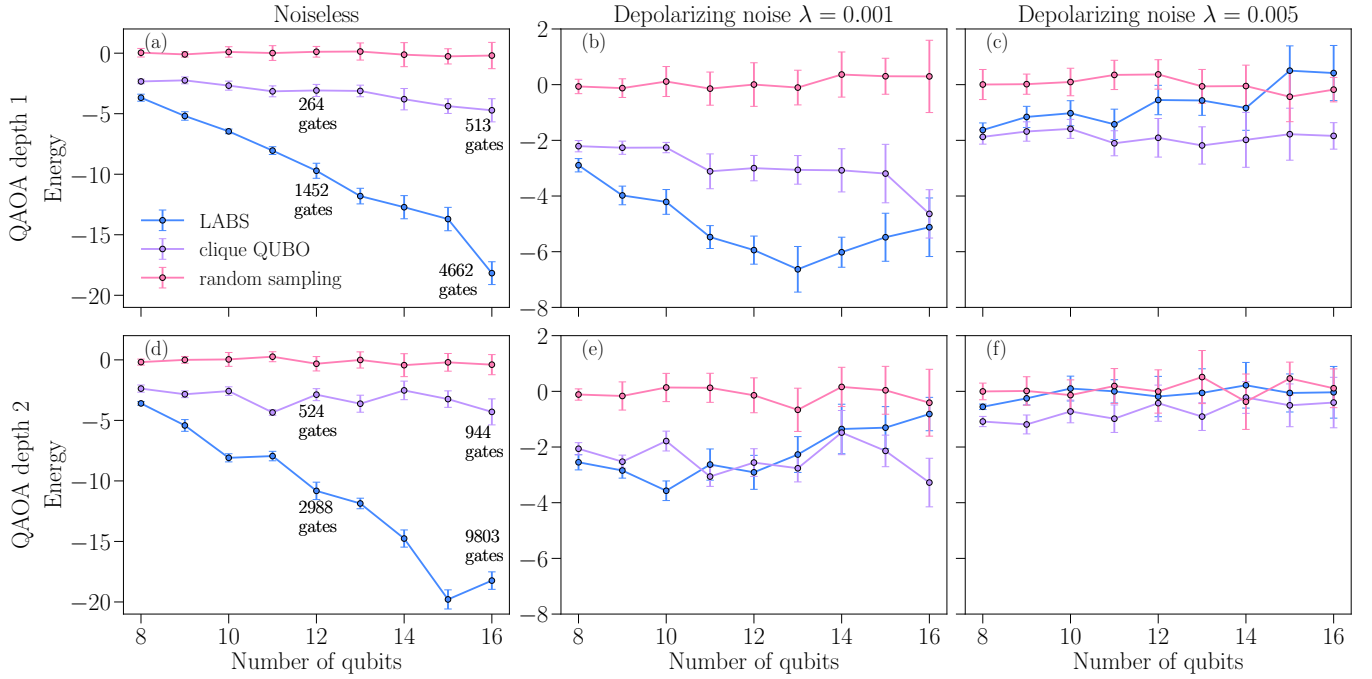


Figure 5. Evolution of expected performance of QAOA for LABS versus problem size, using the standard Ansatz (blue) and the quadratized Ansatz (purple) compared to random sampling (pink). Panels (a-c) correspond to depth-one QAOA with depolarizing noise strengths of 0 (i.e. noiseless), 0.001, and 0.005, respectively. Panels (d-f) show a depth-two QAOA with the same depolarizing noise strengths. The numbers in panels (a) and (d) indicate the number of two-qubit gates in the Ansatz. Each data point is the average of 10 circuit runs and the error bars represent shot noise over 10 000 samples.

to the qubits. Ref. [53] proposes a method to optimize the initial mapping by using a SAT solver. Once the Ansatz is created, we optimize the QAOA parameters by minimizing the energy of the original cost operator

$$\min_{\beta_k, \gamma_k} \langle \psi_k(\beta_k, \gamma_k) | H_C | \psi_k(\beta_k, \gamma_k) \rangle \quad (10)$$

where

$$|\psi_k(\beta_k, \gamma_k)\rangle = \prod_{j=1}^p e^{-i\beta_{j,k} H_M} e^{-i\gamma_{j,k} H_C(k)} |+\rangle^{\otimes n}. \quad (11)$$

Our approach is similar to the time-block Ansatz design presented in Ref. [41]. The main distinction is that a time-block Ansatz assigns different, independently optimized parameters to the edges of $H_C(k)$. Concretely, they replace the values $\gamma_{j,k}$ with corresponding vectors $\{\gamma_{j,k}^e, \forall e \in E\}$.

We benchmark the truncated Ansatz using Max-Cut problems [15] for all $k \in [0, k_{\max}]$. We thus aim to split the set V of n nodes of a graph $G = (E, V)$ into two such that the sum of the edges connecting the two subsets is maximized. Formally, a variable x_i is assigned to each node $i \in V$ to indicate which side of the cut the node is on. Solving Max-Cut is then equivalent to finding the binary string x that maximizes

$$f(x) = \sum_{(j,k) \in E} (x_i(1-x_j) + x_j(1-x_i)). \quad (12)$$

Mapping $f(x)$ to a Hamiltonian [40] results in the cost operator

$$H_{\text{Max-Cut}} = \frac{1}{4} \sum_{(j,k) \in E} Z_i Z_j, \quad (13)$$

with a minimum energy eigenstate that maps to the maximum cut. We measure the quality of a candidate solution x with the approximation ratio

$$r = \frac{f(x)}{\max_x f(x)} \equiv \frac{E_{\max} - E(x)}{E_{\max} - E_{\min}} \in [0, 1], \quad (14)$$

where $E(x) = \langle x | H_C | x \rangle$ is the energy of the basis state $|x\rangle$. The objective value and the energy are related by $2f(x) = |E| - E(x)$. The ground state of $H_{\text{Max-Cut}}$ has $r = 1$. On average, uniformly sampled candidate solutions have $r = 0.5$. The best known polynomial-time randomized rounding algorithm, the Goemans-Williamson algorithm [62], produces samples with $r \simeq 0.878$, on average. For s shots, an average r is computed over the values r_k computed from corresponding bitstrings x_k .

We generate three random three-regular (RR3) graphs with 40 nodes. Each graph can be SAT mapped following Ref. [53] in $k_{\max} = 9$ SWAP layers. Next, we generate an Ansatz circuit with $k \in [0, k_{\max}]$ SWAP layers and depth $p \in \{1, 2, 3\}$. We train the parameters in each Ansatz using MPS simulators to evaluate the energy with a bond dimension of 20, see App. E2 for more de-

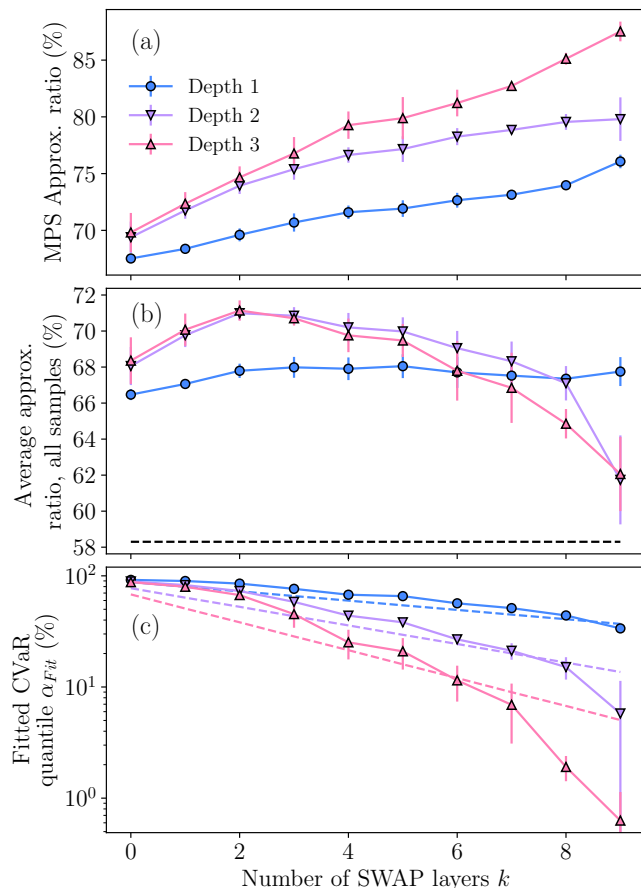


Figure 6. Performance of QAOA as a function of depth and the number of SWAP layers. Each data point is the average of three RR3 graphs that require nine SWAP layers. The error bars show the standard deviation. (a) Approximation ratio of QAOA computed with a MPS evaluation of the energy. (b) Measured approximation ratios from 50 000 samples from *ibm_fez*. The horizontal dashed line is the 58.3% average approximation ratio reported in Ref. [59]. (c) Value of the CVaR quantile α required to make the approximation ratio of the *ibm_fez* samples in (b) match those of the MPS energy evaluation in (a). The dashed lines show a simple theoretical expectation α_{th} based on the two-qubit gate fidelity.

tails. We observe a monotonic increase in the approximation ratio with k evaluated with the MPS, see Fig. 6(a). This shows that the QAOA performance improves as the Ansatz retains more of the problem structure. The circuits are then executed on *ibm_fez* from which we draw 50 000 noisy samples. The samples at $k = 9$ are better than those measured by Sack and Eger on an Eagle device [59], see the black dashed line in Fig. 6(b). This is expected since *ibm_fez* is a Heron device with lower error rates than Eagle devices. Crucially, this data shows significant gains in solution quality when the truncated Ansatz is applied. In the presence of hardware noise, there is an optimal point (k, p) , which represents the maximum depth beyond which increasing either k or p reduces r , see Fig. 6(b). On *ibm_fez*, we find this optimal point at

depth-three with two SWAP layers. Once noise begins to reduce the approximation ratio, the higher depth QAOA degrades faster than the lower depth QAOA.

Increasing k and p increases the differences between the ideal and the hardware results, compare Fig. 6(a) and (b). We can recover a noise-free approximation ratio with the CVaR_α aggregation function [63, 64], which keeps only an $\alpha \in [0, 1]$ fraction of the best samples x measured by $f(x)$. Here, we fit α such that the approximation ratio measured with CVaR_α matches the noiseless one given by the MPS evaluator. The optimization of the alpha parameter is carried out with COBYLA and results in a root mean squared error of 10^{-6} between the 90 MPS approximation ratios and the 90 CVaR ones (three graphs, three depths and ten values of k). As expected, as k and p increase, we discard more shots to recover a noiseless expectation value, see solid lines in Fig. 6(c). This noise strength is then compared to a theoretical amount of noise based on error rates reported by *ibm_fez*. To this end, we compute $\alpha_{\text{th}} = 1/\sqrt{\gamma}$, where γ measures the noise strength of the circuit. We make the simple assumption that

$$\gamma = \gamma_0^{p(2+3\lceil\frac{k}{2}\rceil)} \gamma_1^{p(2+3\lceil\frac{k}{2}\rceil-3)}. \quad (15)$$

Here, γ_0 and γ_1 represent the layer fidelity [65] of the even and odd layer of CZ gates, respectively. The factors γ_i^{2p} account for the first hardware-native layers of R_{ZZ} gates which transpile to four layers of CZ gates per QAOA layer p on *ibm_fez*. The terms $\gamma_0^{3p\lceil\frac{k}{2}\rceil}$ and $\gamma_1^{3p\lceil\frac{k}{2}\rceil-3p}$ account for the even and odd SWAP layers, respectively, which transpile into three layers of CZ gates each. We approximately express the γ_i 's, where $i \in \{0, 1\}$, using the errors $\epsilon_{j,j+1}$ of the native entangling gates between the pairs of qubits j and $j+1$ reported by the backend. For the even and odd layers of two-qubit gates, we have

$$\gamma_i = \prod_{j=0}^{\lfloor\frac{n-1}{2}\rfloor-1} (1 + \epsilon_{2j+i, 2j+i+1}), \quad (16)$$

where the indexing chooses the appropriate two-qubit gate on the line of qubits and we assume $n \geq 3$. This simple $1/\sqrt{\gamma}$ estimation of α already produces excellent qualitative agreement with the fitted α , the solid lines in Fig. 6(c) show the same trend as the dashed ones. At a low number of SWAP layers, we overestimate the sampling overhead since the transpiler removes the unnecessary SWAP gates that the SWAP strategy added. When the circuits become deep, e.g. $k = 9$ and $p = 3$, we tend to underestimate the sampling overhead since we do not account for single-qubit gate noise. In summary, we can (i) trade approximation ratio for a partial implementation of the problem with less noise and (ii) recover a noiseless setting by post-selecting and drawing more samples. This sampling overhead scales exponentially in the circuit depth.

V. DISCUSSION AND CONCLUSIONS

Using noisy quantum hardware to solve non-hardware-native dense optimization problems remains a challenge, which high-order optimization problems exacerbate. For dense four-local Hamiltonians H_4 , the circuit gate count scales as $O(n^4)$. This scaling limits the size of the LABS problem to about 30 decision variables before the noisy hardware samples are effectively random, for a depth-one QAOA and a depolarizing noise strength of $\lambda = 0.001$. This threshold is expected to be even lower for H_4^{full} since it is a denser problem than LABS. We design a scalable Ansatz for high-order optimization problems based on an approximate quadratization of the HUBO using a clique expansion. This construction sacrifices the performance guarantee of QAOA in the $p \rightarrow \infty$ limit, but recovers an Ansatz with a depth linear in problem size n .

The caveat of our procedure lies in the quadratization method. The clique expansion method, originally designed for mathematical applications [55], does not guarantee that the quadratized Hamiltonian preserves the ground state of the original problem. Indeed, an ideal quadratization would ensure that the ground state of the quadratized Hamiltonian and the quartic one coincide. Our approach is, instead, inherently heuristic, and does not come with a theoretical guarantee.

Our simulations confirm that the standard QAOA Ansatz cannot be used in utility-scale applications which inevitably require error correction. Interestingly, they also show that a quadratized Ansatz yields better samples than the standard QAOA Ansatz once a threshold system size, inversely correlated with the noise strength, is reached. The larger the noise strengths, the faster the quadratized Ansatz starts outperforming the standard one in terms of system size. This makes the quadratized Ansatz particularly appealing for today's hardware.

Future work may further investigate on which problems this quadratization approach is expected to be maximally efficient. Furthermore, our approach can be extended by developing hybrid methods that mix our approximate quadratization with an exact implementation of a subset of the high-order terms. Given the large number of gates in dense HUBOs, this strategy may require to exactly implement a considerable amount of gates before yielding a relevant improvement over the direct approximate quadratization. This is because the approximate quadratization assigns weights to the resulting graph edges based on the hyperedges it belonged to. If we exactly implement a small number of hyperedges, the resulting graph will consequently only change very little. In addition, one could choose to exactly quadratize the terms in a subset E' of the fourth order terms as in [54], which would come at a cost of $2|E'|$ qubit overhead.

The second contribution of this paper is designing hardware-friendly Ansätze for QUBOs. We use SWAP Strategies [41, 53, 60, 61] to create a truncated cost Hamiltonian that approximates the target one. We observe that the approximation ratio monotonically in-

creases with the number of SWAP layers k in a noiseless setting. However, this trend changes in the presence of noise, resulting in an optimal pair (k, p) that maximizes the average approximation ratio. In future work, it is worth investigating whether using SWAP Strategies improves the results found in Ref. [41].

Further, optimizing the QAOA variational parameters remains a challenge due to vanishing gradients [8, 66–68], and an abundance of local minima [69]. Thus, solving dense problems with the typical QAOA Ansatz requires significant quantum and classical resources. Progressively building-up the Ansatz and optimizing its parameters one SWAP layer at a time may mitigate this effect. Future work will investigate the effect of additionally optimizing the weights of the truncated QUBO, similarly to how we quadratized HUBOs.

In summary, our work highlights the challenges in implementing high-order optimization problems on quantum hardware. We show how these challenges can be mitigated by carefully designing the Ansatz circuit from which to sample. Moreover, our work points out additional directions in which possible approximate quadratization may further be explored.

VI. ACKNOWLEDGMENTS

The authors acknowledge Stefan Woerner for stimulating discussions. D.J.E. acknowledges funding within the HPQC project by the Austrian Research Promotion Agency (FFG, project number 897481) supported by the European Union – NextGenerationEU. S.D. acknowledges funding from NCCR SwissMAP and the ETH Zurich Quantum Center.

Appendix A: Circuit complexity scaling

1. Fully-connected QUBO two-qubit gate count

We now give some intuition on the number of entangling gates discussed in Section II and depicted in Fig. 1(a). Assuming all-to-all qubit connectivity, implementing all $n(n-1)/2$ R_{ZZ} terms requires $n(n-1)$ entangling two-qubit gates. Assuming linear qubit connectivity, we use SWAP layers to optimally implement a fully-connected QUBO. A SWAP layer contains $\lfloor n/2 \rfloor$ or $\lfloor (n-1)/2 \rfloor$ SWAP gates, depending on its parity. This leads to an additional $\Delta N_{\text{line}} = 3 \times \left[\frac{1}{2}(n-2) \cdot \left(\lfloor n/2 \rfloor + \lfloor (n-1)/2 \rfloor \right) \right]$ entangling two-qubit gates since a SWAP is equivalent to three CNOT gates. When transpiling the final circuit, the overhead gate count becomes $\Delta N_{\text{line}}/3$ due to the cancellation of neighboring entangling gates, i.e. we have only one entangling gate, instead of three, in the addition to the two corresponding to R_{ZZ} in Fig. 7. The asymptotic factor between circuit gate count on linear

and all-to-all connectivity is then

$$\alpha = 1 + \lim_{n \rightarrow \infty} \frac{\Delta N_{\text{line}}/3}{n(n-1)} = 1.5, \quad (\text{A.1})$$

where we add the overhead of entangling gates on top of the constant factor 1, showing that a linear topology requires denser circuits than an all-to-all one. In the $p = 1$ case, the fitted data yields $\alpha = 1.451$.

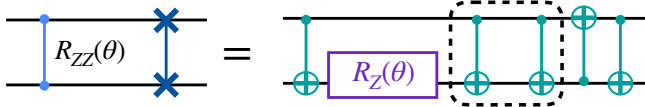


Figure 7. Decomposition of an R_{ZZ} gate followed by a SWAP gate into a basis gate set made of single-qubit rotations and a CX . Here, two consecutive CX gates cancel. This construction is typical in SWAP networks on linear connectivity, see Fig. 2(d).

2. Fully-connected QUBO two-qubit depth

We now rationalize the factor of 1.445 between the circuit depth of a fully-connected QUBO on all-to-all and linear qubit connectivity as seen in Fig. 1(b). A fully-connected QUBO on n variables contains $n(n-1)/2$ terms and is implemented by $n-1$ layers of R_{ZZ} gates with all-to-all connectivity, since each qubit is involved in $n-1$ interactions. Since each R_{ZZ} gate requires two entangling gates, the total two-qubit depth is $2(n-1)$. On a linear qubit connectivity, the same QUBO is optimally implemented using $n-2$ SWAP layers [60]. A SWAP layer has depth three since each SWAP gate is implemented through three entangling gates. In SWAP networks, an R_{ZZ} gate followed by a SWAP gate allows us to simplify to adjacent entangling gates, see Fig. 7. This leads to a total depth of $3(n-2)$ gates. The asymptotic factor between the circuit depth on linear and all-to-all connectivity is then

$$\alpha = \lim_{n \rightarrow \infty} \frac{3(n-2)}{2(n-1)} = 1.5. \quad (\text{A.2})$$

Appendix B: Circuit transpilation

1. HUBOs

Here, we describe how we transpile QAOA circuits for the higher-order problems. We rely on the ‘transpile’ function of Qiskit [48], which decomposes physical operators into the basis gate set $\{R_Z, \sqrt{X}, X, CZ\}$. We assume either the default all-to-all connectivity, or a linear one, by providing a coupling map consisting of a list of connected qubit pairs $[i, i+1]$ and $[i+1, i]$, where

$i \in [0, n-1]$. We set the optimization level to 3. Qiskit will thus route the QAOA circuit to the hardware topology with the LightSABER algorithm [70] which is an enhancement of the SABER SWAP algorithm [71]. Next, the instructions in the routed circuit will be decomposed to hardware native ones and undergo further optimizations to remove, e.g., canceling gates, and SWAPs as well as diagonal gates that occur before measurement instructions.

2. Random three-regular graphs

We now describe the circuit transpilation procedure for the experiments ran on *ibm_fez* for QAOA for RR3 graphs. First, the qubit connectivity and native gate set are provided by the given backend. We then compile Ansatz circuits with SWAP Strategies as described in the publicly available ‘qopt-best-practices’ repository [72]. For QUBOs that are not fully connected, the circuit depth can often be reduced by appropriately mapping the decision variables onto the physical qubits. We use the approach of Matsuo et al. [53], which finds an initial mapping by solving multiple satisfiability (SAT) problems to minimize the number of SWAP layers. This method can become time-consuming since SAT problems are NP-hard. For our experiments, we set a timeout time of 20 seconds. After the circuit is built from R_{ZZ} and SWAP gates, we run the Qiskit transpiler on a low optimization level, i.e. 1, to decompose the gates in CZ gates and simplify any redundant gates.

Appendix C: Weights of quadratized hypergraphs

In this section, we derive an analytical formula for the weights $w_2^{\text{opt}}(j, k)$ of the clique expansion. For now, we consider Hamiltonians which only contain d -local terms. Denote by N_{jk} the number of all hyperedges containing edge (j, k) . From Eq. (7), we can compactly express $w_2^{\text{opt}}(j, k)$. Expanding the binomials and eliminating the constant factors results in

$$\arg \min_{w_2(j,k)} N_{jk} w_2(j, k)^2 - 2w_2(j, k) \sum_{e \in \mathcal{E}(j,k)} w_4(e), \quad (\text{C.1})$$

which is now easy to minimize yielding

$$w_2^{\text{opt}}(j, k) = \sum_{e \in \mathcal{E}(j,k)} w_4(e) / N_{jk}. \quad (\text{C.2})$$

Therefore, the weight of the resulting edges is the mean of the hyperedges it belongs to when the Hamiltonian contains only d -local terms. For H_4^{full} and $w_4(e) \sim \mathcal{N}(0, 1), \forall e \in \mathcal{E}$, we have $w_2^{\text{opt}}(j, k) \sim \mathcal{N}(0, N_{jk}^{-1/2}), \forall (j, k) \in E$.

LABS requires a separate analysis since its Hamiltonian also includes two-local terms. We introduce the variable I_{jk} which is 1 if $Z_j Z_k$ is in H_{LABS} and 0 otherwise.

We then obtain

$$w_2^{\text{opt}}(j, k) = \arg \min_{w_2(j, k)} \left(I_{jk}(w_2(j, k) - 1)^2 + N_{jk}(w_2(j, k) - 2)^2 \right) \quad (\text{C.3})$$

$$= \arg \min_{w_2(j, k)} \left(w_2(j, k)^2(N_{jk} + I_{jk}) - 2w_2(j, k)(2N_{jk} + I_{jk}) \right) \quad (\text{C.4})$$

The step from Eq. (7) to Eq. (C.3) uses the fact that all quartic and quadratic terms have weight 2, and 1, respectively. The edge weights for the quadratized LABS are thus

$$w_2^{\text{opt}}(j, k) = 2 - \frac{I_{jk}}{N_{jk} + I_{jk}}. \quad (\text{C.5})$$

The resulting weights $w_2^{\text{opt}}(j, k)$ are close to 2 since $I_{jk} \in \{0, 1\}$ and $N_{jk} \sim O(n)$. To see why $N_{jk} \sim O(n)$, consider another pair of nodes (h, l) with which the edge (j, k) could form a hyperedge $e = (j, k, h, l)$. The expected value of N_{jk} is the sum of the probabilities that the tuple (j, k, h, l) forms a hyperedge in the original hypergraph \mathcal{E} , for all pairs of nodes $h, l \in V$, i.e.

$$\mathbb{E}(N_{jk}) = \sum_{h, l \in V} \text{Prob}[(j, k, h, l) \in \mathcal{E}] \quad (\text{C.6})$$

Since LABS has $O(n^3)$ four-local terms and there are $O(n^4)$ total possible four-local terms, then $\text{Prob}[(j, k, h, l) \in \mathcal{E}] \sim O(1/n)$ for an arbitrary pair of nodes (h, l) . Further, there are $O(n^2)$ ways of choosing the nodes (h, l) , thus yielding $\mathbb{E}(N_{jk}) \sim O(n)$.

While the resulting edges have a nearly constant value, they are provably different, thus making the optimization landscape hard to navigate, see Fig. 4. Consider the qubit index parity constraints for the $gates in H_{LABS} from Eq. (5). Since only pairs of qubits $(i, i + 2t)$ appear, then about half of the edges (j, k) will satisfy $I_{jk} = 1$. Similarly, the exact value of N_{jk} will depend on how the values of j, k fit within the qubit indexing constraint for four-local gates $(i, i + t, i + u, i + u + t)$.$

Appendix D: Impact of weight distribution on hypergraph-graph correlations

In this section, we extend the analysis in Section III by exploring depth-one QAOA and the energy of the states of the original Hamiltonian against the quadratized one for a set of different four-local Hamiltonians. We consider Hamiltonians with the same structure of H_4^{full} and LABS, but different hyperedge weights. We also explore an additional Hamiltonian with random structure H_4^{random} , which we choose as follows: out of all potential

$\binom{n}{4}$ four-body interaction terms, we randomly choose n^3 . For each Hamiltonian structure, we tested three different hyperedge weight distributions: normal $\mathcal{N}(0, 1)$, uniform in $[0, 1]$, and constant with weight 1. Additionally, we also refer to the LABS problem as having constant weights since all of its four-local terms have weight 2, and all of its two-local terms have weight 1.

The distribution of the hyperedge weights defines the shape of the resulting scatter plot by limiting the possible configuration energies of the quadratized Hamiltonian. The hyperedge weight distribution affects the QUBO edge weight distribution, which in turn defines the possible QUBO energies. When the weights of the hyperedges are constant and there are enough hyperedges for the projection to result in a fully connected QUBO, the set of all possible QUBO energies is limited to $\lceil (n + 1)/2 \rceil$ values, see first column of Fig. 8. Each possible energy is determined by the Hamming weight $0 \leq h \leq n$ and $n - h$ of the basis state, since an unweighted fully-connected QUBO is invariant under a permutation of its decision variables. To see this, consider the fully connected QUBO $w \sum_{i, j} Z_i Z_j$ with equal weights w . Next, consider a basis state of n qubits in binary form $|b\rangle = |b_{n-1}, \dots, b_0\rangle$ with $b_i \in \{0, 1\}$. A permutation of the b_i 's conserves the Hamming weight. Furthermore, this permutation is a unitary matrix that leaves $w \sum_{i, j} Z_i Z_j$ invariant since the edges have equal weights and it is fully-connected. Therefore, a dense enough four-local Hamiltonian with constant hyperedge weights will have quartic energies organized in vertical clusters, see Figs. 8(a) and (g). The small deviations in Fig. 8(d) are due to the additional two-local terms of the LABS structure which leads to different QUBO edge weights, see App. C.

Similarly, for uniformly distributed hyperedge weights, the energy spectrum of the quadratized Hamiltonian forms multiple clusters centered around the QUBO energies given by a constant-weight QUBO, see Figs. 8(b), (e) and (h). The deviation from the vertical clusters identified in the constant hyperedge weight case can be estimated through the deviation of the resulting edge weights from their mean. According to Eq. (C.2), the edge weight $w_2^{\text{opt}}(j, k)$ is the mean of the weights of the hyperedges containing (j, k) . Next, the Central Limit Theorem states that the distribution of a statistical sample of size n , where each variable has average μ and variance σ^2 , can be approximated in the limit $n \rightarrow \infty$ with a normal distribution with mean μ and variance $n \cdot \sigma^2$. Thus, $w_2^{\text{opt}}(j, k)$ follows a normal distribution with average 0.5 and standard deviation $\sqrt{N/12}$, where $(1/12)$ represents the variance of the hyperedge weights sampled from a uniform distribution on the interval $[0, 1]$, and N is the number of hyperedges that contain (j, k) . For 12 qubits, we have the $\max(N) = \binom{10}{2} = 45$, resulting in a maximal standard deviation of $\sigma_{\text{unif}} \approx 1.93$. This is small in comparison to the QUBO energy range $(0, 60)$, thus preserving the vertical clusters, see Figs. 8(b), (e) and (h).

For a standard normal hyperedge weight distribution,

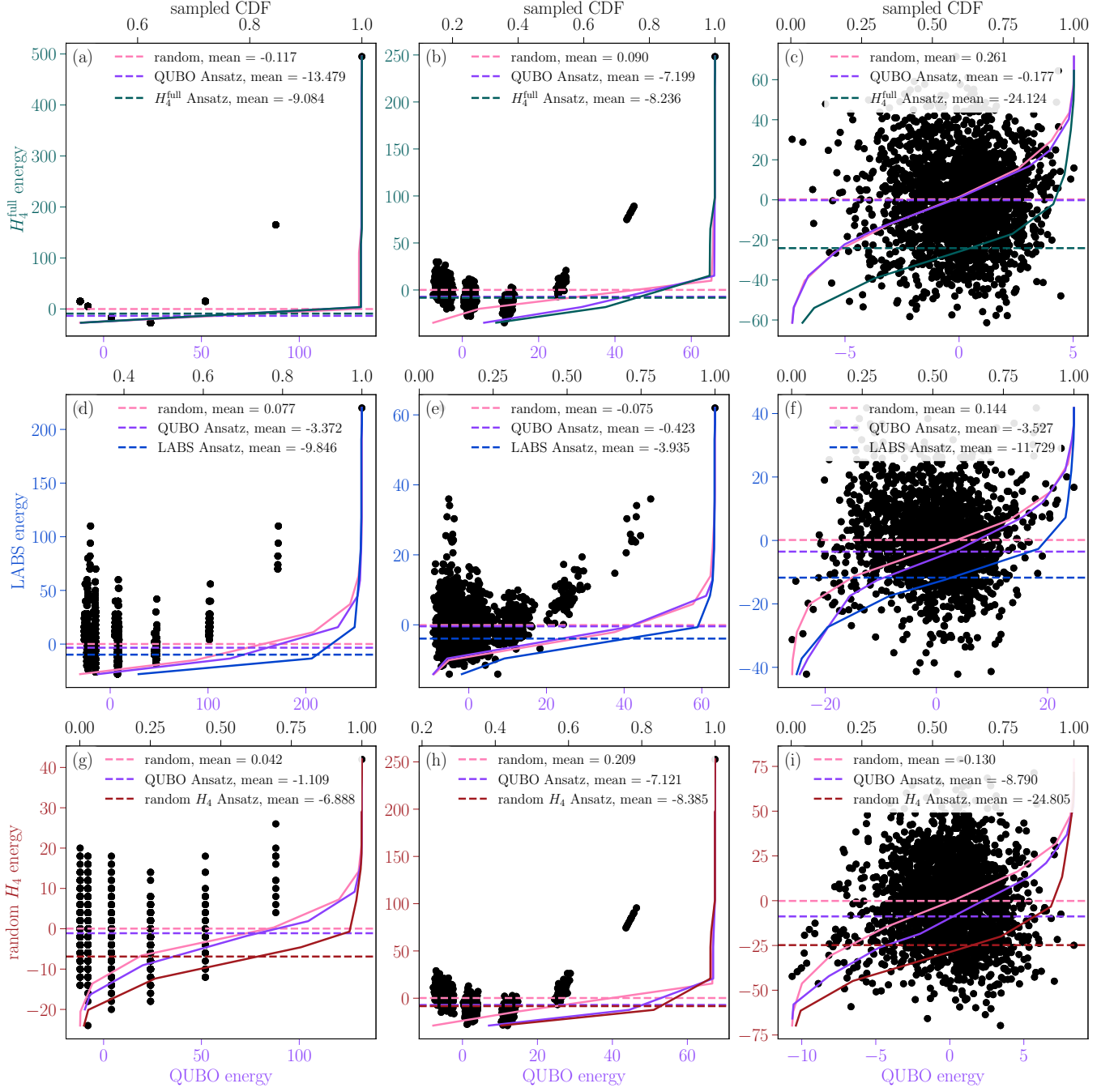


Figure 8. Fourth-order Hamiltonian with 12 qubits. The x - and y -axes show the energy of the quadratized approximate Hamiltonian $\langle H_2 \rangle$, and the original Hamiltonian $\langle H_4 \rangle$, respectively, for the 2^{12} states. The curves show the Cumulative Distribution Function (CDF) of the quartic energies of uniform samples (pink), and samples from running QAOA with the quadratized Ansatz (purple), and the standard Ansatz. The horizontal lines show the corresponding mean energies of these distributions. The hyperedge weights are constant in (a, d, g), chosen uniformly from $[0, 1]$ in (b, e, h), and normally distributed with mean 0 and standard deviation 0 in (c, f, i). The Hamiltonians in (a, b, c) have fourth-order terms only and are fully connected. The Hamiltonians in (d, e, f) have the same structure as LABS. The Hamiltonians in (g, h, i) have n^3 fourth-order terms sampled at random from all possible four-local terms. Panel (c) depicts H_4^{full} with normally distributed hyperedge weights, and Panel (d) the usual LABS problem.

the energies of the resulting QUBO are uncorrelated with the quartic energies, see Figs. 8(c), (h) and (k). This is because the standard deviation of the resulting edge weights, and consequently also of the constant QUBO energies, $\sigma_{\text{normal}} = \sqrt{N} \approx 12.85$, is now large in comparison to the total energy ranges of (0, 5) for the H_4^{full} and random H_4 Hamiltonian, and (0, 20) for the LABS problem.

Furthermore, the quartic Hamiltonian’s structure affects how the black dots are distributed within the vertical clusters determined by the Hamming weights of the corresponding basis states. For the H_4^{full} Hamiltonian, permutation invariance is preserved if the hyperedge weights are all the same. Thus, each vertical cluster corresponds to a single quartic energy, see Fig. 8(a). However, a random Hamiltonian structure does not necessarily exhibit permutation invariance, hence leading to multiple points along a vertical, see Fig. 8(g). The LABS structure also does not have permutation invariance, and additionally exhibits less regularity when compared to only four-local Hamiltonians due to its two-local gates, see Fig. 8(d). At the other extreme, for normally distributed hyperedge weights, and consequently also normally distributed resulting QUBO energies, there is no structural connection between the basis states $\{|x\rangle\}$ that yield the same quadratized energy. Hence, the distribution of quartic energies over a chosen subset $\{|x\rangle\}$ will have the same distribution as the quartic energy over the entire state space, i.e. all $\{|x\rangle\}$, namely normally distributed, see Figs. 8(c), (f) and (i).

The scatter plots show that both problem structure and the distribution of the hyperedge weights impact the energy relation between the quartic and quadratized Hamiltonian. Based on these results, we do not expect good QAOA performance on instances where the energies are unrelated, e.g. Fig. 8(c). We test this expectation by investigating the performance of depth-one QAOA as measured by its mean energy. The quadratization is thus relevant for the LABS problem and the random H_4 with constant hyperedge weights, where the reduction in mean energy performance is small enough to make it useful on noisy hardware, see Figs. 8(d) and (g). For uniformly distributed hyperedge weights, the QUBO Ansatz performs very well compared to the standard Ansatz for H_4^{full} and the random H_4 structure, i.e. the mean energies of the QUBO Ansatz are -7.20 and -7.121 compared to -8.236 and -8.385 for the standard Ansatz, respectively, see Figs. 8(b) and (h). However, for a problem with the same structure as LABS but with uniformly sampled edge weights, we hardly see any improvement of a quadratized Ansatz over random sampling, see Fig. 8(e). If the hyperedge weights are normally distributed, then the problem structure is lost through the quadratization when working with a fully dense quartic Hamiltonians, see Fig. 8(c). However, when the problem is not completely dense, we observe that the quadratized Ansatz performs better than random sampling but worse than depth-one QAOA with an Ansatz based on the full

problem, see Figs. 8(f) and (i).

These simulations show that building an Ansatz based on a quadratization has value if some of the problems structure is retained. Crucially, we see that both the structure of the quartic Hamiltonian and the weights of hyperedges play a role.

Appendix E: Parameter optimization procedure

1. HUBOs

We now discuss our parameter optimization procedure for HUBOs. For depth-one QAOA, we scan the 2D grid $\beta, \gamma \in [0, \pi/2]$ with 60 points, see Fig. 9. Even for the small systems sizes we consider, the optimization landscapes have many local minima, making them hard to explore. Additionally, the standard QAOA Ansatz exhibit fast oscillating features that change with the system size, see Figs. 9(a-e) and (k-o). However, while the Ansatz based on the quadratization also display energy landscapes with many local minima, they appear to be qualitatively different from their quartic counterparts, see Figs. 9(f-j) and (p-t). In particular, the energy landscapes of the quadratized Ansatz seem to indicate parameter concentration at larger system sizes.

Based on initial scans, we fix the area of interest to the top left square $\beta \in [1.4, \pi/2]$ and $\gamma \in [0, 0.3]$ and do a finer search with 100 points per axis for 6 variables. The QAOA parameters for LABS problems with $n > 6$ variables are optimized with SciPy [73] using COBYLA with an initial point given by the optimal β and γ of the problem with $n - 1$ variables. We set the ‘rhobeg’ parameter, which determines the scale of the first gradient step, to 0.1 to qualitatively match the feature size of the energy landscapes, see Figs. 4 and 9.

For QAOA depth $p > 1$ a parameter scan is no longer possible. Therefore, we optimize the parameters in the quadratized Ansatz using transition states [74]. Since we consider systems with at most 16 qubits, which are still simulable, we use the Qiskit statevector simulator to exactly simulate the system and consequently ensure the parameter optimization does not suffer from shot-noise.

2. Random three-regular graphs

The parameter optimization for QAOA when solving the Max-Cut problem on RR3 is still challenging, despite working with a problem with smaller locality than a fully-connected QUBO. However, since this problem has been much more studied in the literature, there are multiple initialization strategies and performance guarantees [23, 33, 56, 74–76].

Similarly as for HUBOs, at depth-one QAOA, we scan the 2D grid $\beta, \gamma \in [0, \pi/2]$ with 60 points. However, unlike HUBOs, the standard QAOA Ansatz of QUBOs do not exhibit fast oscillating features as we change the

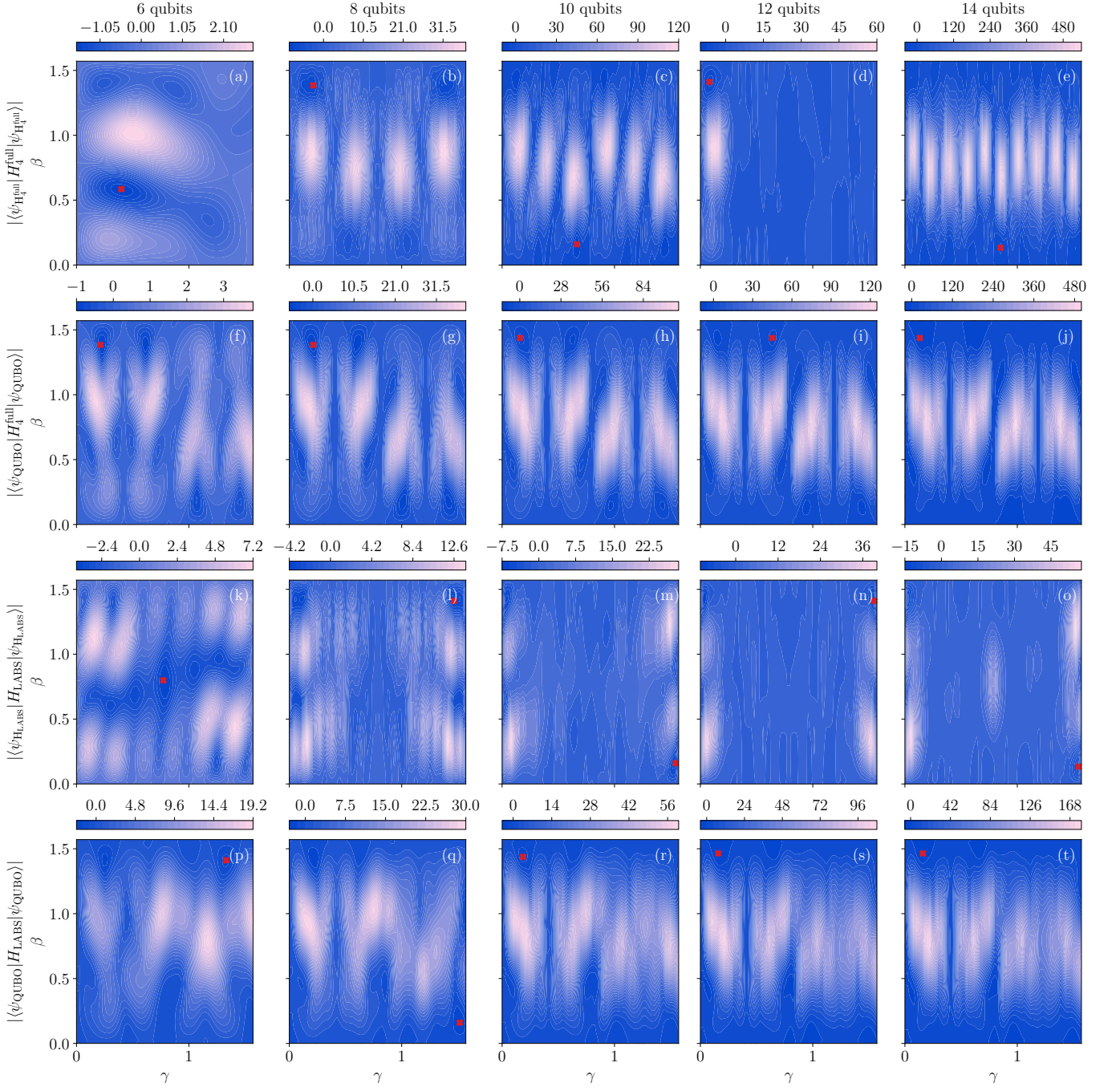


Figure 9. Evolution of parameter optimization landscapes with system size for $n \in \{6, 8, 10, 12, 14\}$. Top two rows show the H_4^{full} energy when using the standard Ansatz and the QUBO Ansatz, respectively. Last two rows show the LABS energy when using the standard Ansatz and the QUBO Ansatz, respectively. Red dots show the absolute minimum found through a grid scan with 60 values per axis.

system size, allowing for a more precise landscape exploration and parameter concentration guarantees [56].

For larger-depth QAOA, we optimize parameters with three initialization methods, and choose the (β, γ) that yield the lowest energy. We compare the Fourier method [23, 75], the Trotterized Quantum Annealing method [76], and transition states method [74].

The RR3 graph instances we investigate have 40 nodes, which prevents a statevector simulation of the underlying quantum circuits without high-performance computing. Hence, we use a QAOA tailored MPS-based simulator which approximates the energy. The MPS simulator relies on the methods described in Ref. [77]. Specifically, the initial state is represented as an MPS with bond di-

mension 1. Single-qubit gates are applied by contracting them with the corresponding tensor in the MPS. Nearest-neighbor two-qubit gates are applied by contracting together the MPS tensors associated with the qubits onto which the gate is applied, contracting the resulting tensor with the gate, and restoring the MPS format through singular value decomposition. Non-nearest-neighbor two-qubit gates are simulated as they are executed in the

hardware, i.e. by using SWAP layers to bring qubits close to each other. The simulator encodes the MPS in the inverse Vidal form [78] to avoid tracking the MPS canonization during the simulation. The quality of the approximation is controlled by the maximum dimension of the tensors composing the MPS, i.e. the bond dimension. For all our simulations, we set the bond dimension to 20 [79].

-
- [1] P. W. Shor, in *Proceedings 35th annual symposium on foundations of computer science* (IEEE, 1994) p. 124–134.
- [2] A. Peruzzo, J. McClean, P. Shadbolt, M.-H. Yung, X.-Q. Zhou, P. J. Love, A. Aspuru-Guzik, and J. L. O’Brien, *Nat. Commun.* **5**, 4213 (2014).
- [3] J. Tilly, H. Chen, S. Cao, D. Picozzi, K. Setia, Y. Li, E. Grant, L. Wossnig, I. Rungger, G. H. Booth, *et al.*, *Phys. Rep.* **986**, 1–128 (2022).
- [4] Y. Cao, J. Romero, and A. Aspuru-Guzik, *IBM J. Res. Dev.* **62**, 6:1–6:20 (2018).
- [5] N. S. Blunt, J. Camps, O. Crawford, R. Izsák, S. Leontica, A. Mirani, A. E. Moylett, S. A. Scivier, C. Sunderhauf, P. Schopf, *et al.*, *J. Chem. Theory Comput.* **18**, 7001–7023 (2022).
- [6] A. Kandala, A. Mezzacapo, K. Temme, M. Takita, M. Brink, J. M. Chow, and J. M. Gambetta, *Nature* **549**, 242–246 (2017).
- [7] P. K. Barkoutsos, J. F. Gonthier, I. Sokolov, N. Moll, G. Salis, A. Fuhrer, M. Ganzhorn, D. J. Egger, M. Troyer, A. Mezzacapo, *et al.*, *Phys. Rev. A* **98**, 022322 (2018).
- [8] Z. Holmes, K. Sharma, M. Cerezo, and P. J. Coles, *Phys. Rev. X Quantum* **3**, 010313 (2022).
- [9] L. L. Peterson and S. B. Davie, *Computer Networks* (Elsevier, 2020).
- [10] H. M. Markowitz, *Portfolio Selection: Efficient Diversification of Investments* (Yale University Press, 1959).
- [11] D. J. Egger, C. Gambella, J. Mareček, S. McFaddin, M. Mevissen, R. Raymond, A. Simonetto, S. Woerner, and E. Yndurain, *IEEE Trans. Quantum Eng.* **1**, 1–24 (2020).
- [12] K. Domino, A. Kundu, Ö. Salehi, and K. Krawiec, *Quantum Inf. Process.* **21**, 337 (2022).
- [13] B. Pascariu, M. Sama, P. Pellegrini, A. D’Ariano, J. Rodriguez, and D. Pacciarelli, *J. Rail Transp. Plan. Manag.* **31**, 100460 (2024).
- [14] A. Sbihi and R. W. Eglese, *Ann. Oper. Res.* **175**, 159–175 (2010).
- [15] R. M. Karp, *Networks* **5**, 45–68 (1975).
- [16] D. Zuckerman, *SIAM J. Comput.* **25**, 1293–1304 (1996).
- [17] A. Abbas, A. Ambainis, B. Augustino, A. Bärttschi, H. Buhrman, C. Coffrin, G. Cortiana, V. Dunjko, D. J. Egger, B. G. Elmegreen, *et al.*, *Nat. Rev. Phys.* **6**, 718–735 (2024).
- [18] E. Farhi, J. Goldstone, and S. Gutmann (2014) [arXiv:1411.4028](https://arxiv.org/abs/1411.4028).
- [19] K. Blekos, D. Brand, A. Ceschini, C.-H. Chou, R.-H. Li, K. Pandya, and A. Summer, *Phys. Rep.* **1068**, 1–66 (2024).
- [20] A. B. Fennila, M. A. Gomez, C. Sebenik, C. Stenson, and J. D. Doll, *Chem. Phys. Lett.* **219**, 343–348 (1994).
- [21] A. Rajak, S. Suzuki, A. Dutta, and B. K. Chakrabarti, *Philos. Trans. R. Soc., A* **381**, 20210417 (2023).
- [22] T. Koch, D. E. Bernal Neira, Y. Chen, G. Cortiana, D. J. Egger, R. Heese, N. N. Hegade, A. G. Cadavid, R. Huang, T. Itoko, *et al.* (2025) [arXiv:2504.03832](https://arxiv.org/abs/2504.03832).
- [23] L. Zhou, S.-T. Wang, S. Choi, H. Pichler, and M. D. Lukin, *Phys. Rev. X* **10**, 021067 (2020).
- [24] S. Brandhofer, D. Braun, V. Dehn, G. Hellstern, M. Hüls, Y. Ji, I. Polian, A. S. Bhatia, and T. Wellens, *Quantum Inf. Process.* **22**, 25 (2022).
- [25] M. Willsch, D. Willsch, F. Jin, H. De Raedt, and K. Michielsen, *Quantum Inf. Process.* **19**, 1–24 (2020).
- [26] G. C. Santra, F. Jendrzejewski, P. Hauke, and D. J. Egger, *Phys. Rev. A* **109**, 012413 (2024).
- [27] R. Tate, J. Moondra, B. Gard, G. Mohler, and S. Gupta, *Quantum* **7**, 1121 (2023).
- [28] D. J. Egger, J. Mareček, and S. Woerner, *Quantum* **5**, 479 (2021).
- [29] D. Rehfeldt, T. Koch, and Y. Shinano, *Math. Program. Comput.* **15**, 445–470 (2023).
- [30] D. Gamarnik, *Proc. Natl. Acad. Sci. U. S. A.* **118**, e2108492118 (2021).
- [31] D. Lykov, R. Shaydulin, Y. Sun, Y. Alexeev, and M. Pistoia, in *Proceedings of the SC’23 Workshops of The International Conference on High Performance Computing, Network, Storage, and Analysis* (2023) p. 1443–1451.
- [32] D. Lykov, J. Wurtz, C. Poole, M. Saffman, T. Noel, and Y. Alexeev, *Npj Quantum Inf.* **9**, 73 (2023).
- [33] V. Akshay, H. Philathong, M. E. Morales, and J. D. Biamente, *Phys. Rev. Lett.* **124**, 090504 (2020).
- [34] S. V. Romero, A.-M. Visuri, A. G. Cadavid, E. Solano, and N. N. Hegade (2024) [arXiv:2409.04477](https://arxiv.org/abs/2409.04477).
- [35] J. Brest and B. Bošković, *IEEE Access* **9**, 67713–67723 (2021).
- [36] T. Packebusch and S. Mertens, *J. Phys. A: Math. Theor.* **49**, 165001 (2016).
- [37] R. Shaydulin, C. Li, S. Chakrabarti, M. DeCross, D. Herman, N. Kumar, J. Larson, D. Lykov, P. Minssen, Y. Sun, *et al.*, *Sci. Adv.* **10**, eadm6761 (2024).
- [38] Gurobi Optimization LLC., <https://www.gurobi.com>.
- [39] IBM ILOG CPLEX. V20.1: User’s manual for cplex, <https://www.ibm.com/docs/en/icos/22.1.2?topic=optimizers-users-manual-cplex>.
- [40] A. Lucas, *Front. Phys.* **2**, 5 (2014).
- [41] F. B. Maciejewski, S. Hadfield, B. Hall, M. Hodson, M. Dupont, B. Evert, J. Sud, M. S. Alam, Z. Wang, S. Jeffrey, *et al.*, *Phys. Rev. A* **22**, 044074 (2024).
- [42] L. Zhu, H. L. Tang, G. S. Barron, F. A. Calderon-Vargas, N. J. Mayhall, E. Barnes, and S. E. Economou, *Phys. Rev. Res.* **4**, 033029 (2022).
- [43] F. G. Fuchs, K. O. Lye, H. M. Nilsen, A. J. Stasik, and

- G. Sartor, *Algorithms* **15**, 202 (2022).
- [44] Z. He, R. Shaydulin, S. Chakrabarti, D. Herman, C. Li, Y. Sun, and M. Pistoia, *Npj Quantum Inf.* **9**, 121 (2023).
- [45] M. Y. Niu, S. Lu, and I. L. Chuang (2019) [arXiv:1905.12134](https://arxiv.org/abs/1905.12134).
- [46] M. Gelay, *IEEE Trans. Inf. Theory* **23**, 43 (1977).
- [47] J. Bernasconi, *J. Phys.* **48**, 559 (1987).
- [48] A. Javadi-Abhari, M. Treinish, K. Krsulich, C. J. Wood, J. Lishman, J. Gacon, S. Martiel, P. D. Nation, L. S. Bishop, A. W. Cross, *et al.* (2024) [arXiv:2405.08810](https://arxiv.org/abs/2405.08810).
- [49] V. Rosenhaus, *J. Phys. A: Math. Theor.* **52**, 323001 (2019).
- [50] Z. Luo, Y.-Z. You, J. Li, C.-M. Jian, D. Lu, C. Xu, B. Zeng, and R. Laflamme, *Npj Quantum Inf.* **5**, 53 (2019).
- [51] B. Kobrin, Z. Yang, G. D. Kahanamoku-Meyer, C. T. O'lund, J. E. Moore, D. Stanford, and N. Y. Yao, *Phys. Rev. Lett.* **126**, 030602 (2021).
- [52] J. Brest and B. Bošković, *IEEE Access* **6**, 4127–4134 (2018).
- [53] A. Matsuo, S. Yamashita, and D. J. Egger, *IEICE Trans. Fundam. Electron. Commun. Comput. Sci.* **106**, 1424 (2023).
- [54] A. Mandal, A. Roy, S. Upadhyay, and H. Ushijima-Mwesigwa, in *Proceedings of the 17th ACM International Conference on Computing Frontiers* (2020) pp. 126–131.
- [55] V. Suppakitpaisarn and J.-K. Hao, in *Metaheuristics International Conference* (Springer, 2024) pp. 219–233.
- [56] V. Akshay, D. Rabinovich, E. Campos, and J. Biamonte, *Phys. Rev. A* **104**, L010401 (2021).
- [57] V. Katial, K. Smith-Miles, C. Hill, and L. Hollenberg, *INFORMS J. Comput.* **37**, 146–171 (2025).
- [58] E. Magesan, J. M. Gambetta, and J. Emerson, *Phys. Rev. Lett.* **106**, 180504 (2011).
- [59] S. H. Sack and D. J. Egger, *Phys. Rev. Res.* **6**, 013223 (2024).
- [60] J. Weidenfeller, L. C. Valor, J. Gacon, C. Tornow, L. Bello, S. Woerner, and D. J. Egger, *Quantum* **6**, 870 (2022).
- [61] M. P. Harrigan, K. J. Sung, M. Neeley, K. J. Satzinger, F. Arute, K. Arya, J. Atalaya, J. C. Bardin, R. Barends, S. Boixo, *et al.*, *Nat. Phys.* **17**, 332–336 (2021).
- [62] M. X. Goemans and D. P. Williamson, *J. ACM* **42**, 1115–1145 (1995).
- [63] P. K. Barkoutsos, G. Nannicini, A. Robert, I. Tavernelli, and S. Woerner, *Quantum* **4**, 256 (2020).
- [64] S. V. Barron, D. J. Egger, E. Pelofske, A. Bäertschi, S. Eidenbenz, M. Lehmkuehler, and S. Woerner, *Nat. Comput. Sci.* **4**, 865–875 (2024).
- [65] D. C. McKay, I. Hincks, E. J. Pritchett, M. Carroll, L. C. G. Govia, and S. T. Merkel (2023) [arXiv:2311.05933](https://arxiv.org/abs/2311.05933).
- [66] M. Larocca, S. Thanasilp, S. Wang, K. Sharma, J. Biamonte, P. J. Coles, L. Cincio, J. R. McClean, Z. Holmes, and M. Cerezo (2024) [arXiv:2405.00781](https://arxiv.org/abs/2405.00781).
- [67] A. Arrasmith, Z. Holmes, M. Cerezo, and P. J. Coles, *Quantum Sci. Technol.* **7**, 045015 (2022).
- [68] J. R. McClean, S. Boixo, V. N. Smelyanskiy, R. Babbush, and H. Neven, *Nat. Commun.* **9**, 4812 (2018).
- [69] L. Bittel and M. Kliesch, *Phys. Rev. Lett.* **127**, 120502 (2021).
- [70] H. Zou, M. Treinish, K. Hartman, A. Ivrii, and J. Lishman (2024) [arXiv:2409.08368](https://arxiv.org/abs/2409.08368).
- [71] G. Li, Y. Ding, and Y. Xie, in *Proceedings of the Twenty-Fourth International Conference on Architectural Support for Programming Languages and Operating Systems*, ASPLOS '19 (Association for Computing Machinery, New York, NY, USA, 2019) p. 1001–1014.
- [72] Qiskit Community, <https://github.com/qiskit-community/qopt-best-practices>.
- [73] P. Virtanen, R. Gommers, T. E. Oliphant, M. Haberland, T. Reddy, D. Cournapeau, E. Burovski, P. Peterson, W. Weckesser, J. Bright, *et al.*, *Nat. Methods* **17**, 261–272 (2020).
- [74] S. H. Sack, R. A. Medina, R. Kueng, and M. Serbyn, *Phys. Rev. A* **107**, 062404 (2023).
- [75] E. Farhi, J. Goldstone, S. Gutmann, and L. Zhou, *Quantum* **6**, 759 (2022).
- [76] S. H. Sack and M. Serbyn, *Quantum* **5**, 491 (2021).
- [77] Y. Zhou, E. M. Stoudenmire, and X. Waintal, *Phys. Rev. X* **10**, 041038 (2020).
- [78] P. Secular, N. Gourianov, M. Lubasch, S. Dolgov, S. R. Clark, and D. Jaksch, *Phys. Rev. B* **101**, 235123 (2020).
- [79] J. Gray, *J. Open Source Softw.* **3**, 819 (2018).